


Determination of the Fermi surface by charge density correlations

Zhipeng Sun *

Beijing Computational Science Research Center, Beijing 100193, China



(Received 4 October 2022; revised 17 April 2023; accepted 18 April 2023; published 27 April 2023)

The Fermi surface topology plays a crucial role in the study of high-temperature superconductivity cuprates. The conventional method for determining the Fermi surface is the maximum spectral intensity method, which involves numerical analytical continuation of Matsubara data for the one-body Green's function. However, the numerical analytical continuation is sensitive to the noise or the precision of the Matsubara data, and hence is not always reliable. With this in mind, we propose a simple and specific notion as a reference for the Fermi surface. It is the derivative of the momentum distribution function n_k with respect to the chemical potential μ . Our analysis of the noninteracting system shows that the momentum, at which $dn_k/d\mu$ takes the maximum value, constitutes a surface, which coincides with the Fermi surface. The relationship between $dn_k/d\mu$ and the Fermi surface in general cases is also analyzed. In order to numerically demonstrate this relationship, we calculate and compare on the two-dimensional Hubbard model within the *HGW* method. The results show that, at least in the weak and intermediate coupling regimes, using the notion of $dn_k/d\mu$ to determine the Fermi surface is reliable. We further studied the cases with model parameters standing for realistic materials, and found the surface determined by $dn_k/d\mu$ exhibits topological transition with the charge filling, similar to the Fermi surface in the cuprates. We believe that using the derivative of the momentum distribution function with respect to the chemical potential to determine the Fermi surface is a reasonable, efficient, and potentially valuable approach.

DOI: [10.1103/PhysRevB.107.165154](https://doi.org/10.1103/PhysRevB.107.165154)

I. INTRODUCTION

For the past century, the concept of the Fermi surface (FS) has played a pivotal role in our understanding of the physical properties of solid-state materials. For conventional metals that can be described by Landau's Fermi liquid theory, the FS can be obtained from the local density approximation calculations, and the results are in good agreement with the experiments. However, in high-temperature superconductivity cuprates (HTSCs), the FS is not well defined due to the failure of the quasiparticle picture [1]. Instead, the Luttinger surface [2], defined through Luttinger's theorem, is taken as the underlying FS [3], also commonly referred to as the FS. Experimental determination of the FS is typically based on data obtained from angle-resolved photoemission spectroscopy (ARPES) measurements [4–6], and the FS of HTSC exhibits topological changes with the charge fillings [7,8]. These features are believed to be linked to strong correlated effects such as the pseudogap and superconductivity [9–12], but their relationship remains a mystery. Therefore, numerical calculations of FS topology in strongly correlated systems have become an important research topic.

In numerical studies, the FS is usually determined by the zero-frequency spectral intensity [13,14], which requires the use of the numerical analytical continuation (NAC) procedure [15,16] on the data of the Matsubara Green's function. However, NAC is sensitive to the noise or the precision of the Matsubara data, and, as a result, it is not always a reliable method. Hence, a method to de-

termine the FS without NAC is desirable for numerical calculations.

In this paper, we propose using the derivative of the momentum distribution function with respect to the chemical potential, $dn_k/d\mu$, as a means to determine the effective FS. We demonstrated the rationale and effectiveness of this approach both theoretically and numerically, at least in the weak and intermediate coupling regimes. We used this approach to calculate the effective FS of the two-dimensional (2D) Hubbard model in correlated regimes and found that it exhibits topological changes with charge filling, similar to the FS observed in cuprates. These calculations were performed using the *HGW* method [17]. Therefore, we believe that the use of the $dn_k/d\mu$ notion to determine the FS in correlated systems is a reasonable, efficient, and potentially valuable approach.

This paper is organized as follows. In Sec. II, we introduce the notion of $dn_k/d\mu$, and demonstrate its relationship with the spectral function $A(\omega, \mathbf{k})$. Then in Sec. III, we introduce our testing solver in the 2D Hubbard model, and numerically verify the validity of the effective FS. After that, we apply our notion to study the FS topological transition for correlated systems in Sec. IV. Our results are summarized in Sec. V.

II. EFFECTIVE FERMION SURFACE AND ITS PHYSICAL MEANINGS

Consider a noninteracting Fermi system at finite temperature $T = 1/\beta$, the momentum distribution function n_k is given by

$$n_k = \frac{2}{1 + e^{\beta(\epsilon_k - \mu)}}. \quad (1)$$

*zpsun@csrc.ac.cn

The FS is where $\varepsilon_k = \mu$ and thus where $n_k = 1$. From Eq. (1), we directly obtain

$$\frac{dn_k}{d\mu} = -\frac{1}{2}\beta n_k^2 + \beta n_k. \quad (2)$$

Obviously, $dn_k/d\mu$ reaches its maximum where $n_k = 1$. Therefore, FS is where $dn_k/d\mu$ reaches its maximum.

For interacting cases, FS typically refers to the Luttinger surface, which can be determined by the maximum of spectral intensity $A_k(\omega; \mu)$ at zero frequency $\omega = 0$. It is worth noting that there is a relationship between n_k and $A_k(\omega; \mu)$ given by the following equation:

$$n_k = 2 \int_{-\infty}^{+\infty} d\omega \frac{A_k(\omega; \mu)}{e^{\beta\omega} + 1}. \quad (3)$$

The spectral function takes the form:

$$A_k(\omega; \mu) = \sum_{N, \alpha, \gamma} \rho_{N, \alpha} |M_{k, N, \alpha, \gamma}|^2 \times \delta[\omega - (E_{N+1, \gamma} - E_{N, \alpha} - \mu)]. \quad (4)$$

Here $(N, E_{N, \alpha})$ are eigenvalues of the total particle number operator \hat{N} and the Hamiltonian \hat{H} , respectively. $\rho_{N, \alpha} = e^{-\beta(E_{N, \alpha} - \mu N)} / Z$ and $Z = \sum_{N, \alpha} e^{-\beta(E_{N, \alpha} - \mu N)}$. Since $M_{k, N, \alpha, \gamma}$ is independent of μ , the derivative of $A_k(\omega; \mu)$ with respect to μ contains two parts:

$$D_1 = \sum_{N, \alpha, \gamma} \frac{d\rho_{N, \alpha}}{d\mu} |M_{k, N, \alpha, \gamma}|^2 \times \delta[\omega - (E_{N+1, \gamma} - E_{N, \alpha} - \mu)], \quad (5)$$

and

$$D_2 = \sum_{N, \alpha, \gamma} \rho_{N, \alpha} |M_{k, N, \alpha, \gamma}|^2 \times \delta'[\omega - (E_{N+1, \gamma} - E_{N, \alpha} - \mu)]. \quad (6)$$

If $\frac{d\rho_{N, \alpha}}{d\mu} = \beta(N - \langle N \rangle)\rho_{N, \alpha}$ is negligible, we can focus only on the contribution of D_2 to $dn_k/d\mu$, leading to the following expression:

$$\frac{dn_k}{d\mu} \approx 2\beta \int_{-\infty}^{+\infty} d\omega A_k(\omega; \mu) \text{sech}^2\left(\frac{\beta\omega}{2}\right). \quad (7)$$

When the value of β is large, the function $f(\omega) = \beta \text{sech}^2(\beta\omega/2)$ becomes sharply peaked at $\omega = 0$ and approximately resembles a Dirac δ function. Subsequently, Eq. (7) can be simplified to:

$$\frac{dn_k}{d\mu} \approx 2A_k(\omega = 0; \mu). \quad (8)$$

That means the derivative of n_k with respect to μ is proportional to the zero-frequency spectral intensity. In other words, the surface determined by the maximum of $dn_k/d\mu$ will be similar to FS determined by the maximum spectral intensity.

We now consider the physical interpretation of $dn_k/d\mu$. First, its definition describes the rate of change of the momentum distribution function n_k with respect to the chemical potential μ , suggesting that the most active particles are located where $dn_k/d\mu$ is the largest, potentially representing the Fermi surface. Second, averaging $dn_k/d\mu$ over all momenta

\mathbf{k} yields the charge compressibility $\chi^c = dn/d\mu$, making $dn_k/d\mu$ the momentum-dependent compressibility. Finally, $dn_k/d\mu$ can be expressed as:

$$\frac{dn_k}{d\mu} = \sum_{k'} \int_0^\beta d\tau' \langle n_k(\tau = 0) n_{k'}(\tau') \rangle - \langle n_k(\tau = 0) \rangle \sum_{k'} \int_0^\beta d\tau' \langle n_{k'}(\tau') \rangle. \quad (9)$$

It reflects the correlation between the \mathbf{k} -specified charge density and the total charge density, potentially serving as a bridge between the Fermi surface and charge correlation functions.

III. NUMERICAL VERIFICATION FOR VALIDITY OF EFFECTIVE FERMI SURFACE

A. Model and testing solver

We focus on the 2D Hubbard model on a square lattice, whose Hamiltonian is given by

$$\mathcal{H} = - \sum_{ij\sigma} t_{ij} \hat{c}_{i\sigma}^\dagger \hat{c}_{j\sigma} + \frac{U}{2} \sum_{i\sigma} \hat{n}_{i\sigma} \hat{n}_{i\bar{\sigma}} - \mu \sum_{i\sigma} \hat{n}_{i\sigma}. \quad (10)$$

Here $\hat{c}_{i\sigma}^\dagger$ ($\hat{c}_{i\sigma}$) is the creation (annihilation) operator for the electron with spin σ at lattice site i , and $\hat{n}_{i\sigma} \equiv \hat{c}_{i\sigma}^\dagger \hat{c}_{i\sigma}$ is the density operator. t_{ij} is hopping strength for the electron from site i to site j , U is the on-site repulsive interaction, and μ is the chemical potential. Here we only consider the nearest-neighbor hopping strength t and the next-nearest-neighbor hopping strength t' , and set $t = 1$ as the unit of energy. The noninteracting dispersion is given by

$$\varepsilon_k = -2t(\cos k_x + \cos k_y) - 4t' \cos k_x \cos k_y. \quad (11)$$

We employ the *HGW* method as the testing solver to obtain the Green's function due to its low computational complexity and its ability to qualitatively describe the pseudogap. Although the results for the gap and the temperature for the onset of pseudogap are highly overestimated (see Appendix B), traditional approaches like the *GW* approximation and the fluctuation-exchange (FLEX) approximation fail to capture the pseudogap physics. While other many-body methods, such as the two-particle self-consistent (TPSC) theory [18], can be used as the testing solvers in principle.

The *HGW* method is a many-body approach based on the truncation of correlation functions in the Dyson-Schwinger equations. It can be applied to various systems, including the Hubbard model. The *HGW* equations for the Green's function in the Hubbard model are as follows:

$$G_\sigma^{-1}(k) = H_\sigma^{-1}(k) + \frac{1}{\beta L^2} \sum_q H_\sigma(k+q) W_{\sigma\bar{\sigma}}(q), \quad (12)$$

$$[W^{-1}]_{\sigma\sigma'}(q) = \frac{1}{U} \delta_{\sigma\sigma'} - \frac{\delta_{\sigma\sigma'}}{\beta L^2} \sum_k H_{\bar{\sigma}}(k+q) G_\sigma(k), \quad (13)$$

with

$$H_\sigma^{-1}(k) = -ik^0 + (\varepsilon_k - \mu) - \frac{U}{\beta L^2} \sum_p G_{\bar{\sigma}}(p). \quad (14)$$

The index k here denotes a combination of the Matsubara frequency ik^0 and the quasimomentum \mathbf{k} , and L^2 is the total

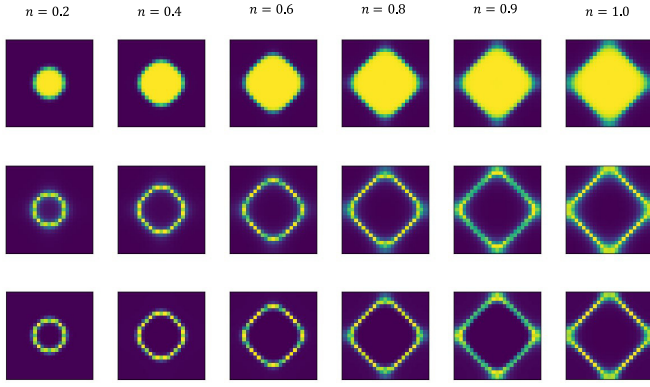


FIG. 1. The figure shows the momentum distribution function n_k (top), zero-frequency spectral intensity $A_k(\omega = 0)$ (middle), and momentum-dependent compressibility $dn_k/d\mu$ (bottom) for weak coupling $U = 2.0$. The results are presented for different fillings from left to right, ranging from 0.2–1.0.

number of lattice sites. $G_\sigma(k)$ represents the one-body Green's function, $W_{\sigma\sigma'}(q)$ acts as the effective dynamical two-body potential, and $H_\sigma(k)$ denotes the noninteracting Green's function with the Hartree self-energy included.

Numerically, the set of Eqs. (12), (13), (14) can be quickly solved by Broyden iterations and fast Fourier transformation algorithms. For each iteration, the computational complexity is of order $ML^2 \log ML^2$, where M is the number of Matsubara time slices. After solving the Green's function $G_\sigma(k)$, we use the Nevanlinna analytical continuation technique [16], which is efficient for noiseless Matsubara Green's function data, to calculate the spectral function, and then obtain the FS by the maximum spectral intensity method.

B. Comparison of two surfaces at weak and intermediate coupling

In Ref. [19], the Fermi surface was simulated for the 24×24 Hubbard model at weak and intermediate couplings ($U = 2.0, 4.0$) and different fillings. Here, we use the *HGW* method to calculate the momentum distribution n_k , the spectral function $A_k(\omega)$, and the momentum-dependent compressibility $dn_k/d\mu$ for the same parameters. This serves as a numerical verification of the similarity between the two surfaces and also tests the validity of the *HGW* method.

Figures 1 and 2 present plots of the momentum distribution function n_k , the zero-frequency spectral intensity $A_k(\omega = 0)$, and the momentum-dependent compressibility $dn_k/d\mu$ for the 2D square Hubbard model with interaction strengths $U = 2.0$ and $U = 4.0$, respectively. The results show that the two surfaces determined by $A_k(\omega = 0)$ and $dn_k/d\mu$ are almost identical, providing a numerical verification of the similarity between them and the validity of determining the FS by the momentum-dependent compressibility $dn_k/d\mu$.

IV. SURFACE TOPOLOGICAL TRANSITION FOR CORRELATED SYSTEM

A. Numerical results of effective FS

We investigate the $U = 6.0$ and $t' = -0.25$ parameter regime, which corresponds to correlated materials studied in

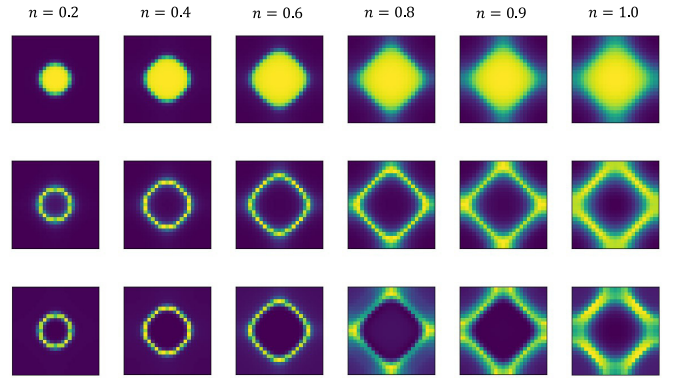


FIG. 2. The plot shows the momentum distribution function n_k (top), zero-frequency spectral intensity $A_k(\omega = 0)$ (middle), and momentum-dependent compressibility $dn_k/d\mu$ (bottom) at intermediate coupling $U = 4.0$. The fillings range from 0.2–1.0 from left to right, and the temperature is $1/5.0$ for $n = 1.0$ and $1/8.0$ for other fillings.

Ref. [20] for evidence of strange metallicity using DQMC simulations. We present the plots of $dn_k/d\mu$ for different fillings and temperatures in Fig. 3, and we provide the plots of FS determined by the maximum spectral intensity method for comparison in Appendix B. The results indicate that the surface has a holelike feature in the overdoped region ($n = 0.7, 0.85$) and a small arc in the underdoped region ($n = 0.9, 0.95$), which is qualitatively similar to the FS in the cuprates [21,22]. Notably, at $n = 1.0$, $1/T = 3.0$, where the system is nearly in the Mott phase, the surface matches qualitatively with the remnant Fermi surface of the Mott insulator $\text{Ca}_2\text{CuO}_2\text{Cl}_2$ [23]. However, we do not observe any indication of the hole pocket that has been reported in experiments [24] or predicted by certain theoretical studies [25–27].

To assess the quality of the obtained Fermi arc, we compare it with experimental results on $\text{Ca}_{2-x}\text{Na}_x\text{CuO}_2\text{Cl}_2$ from

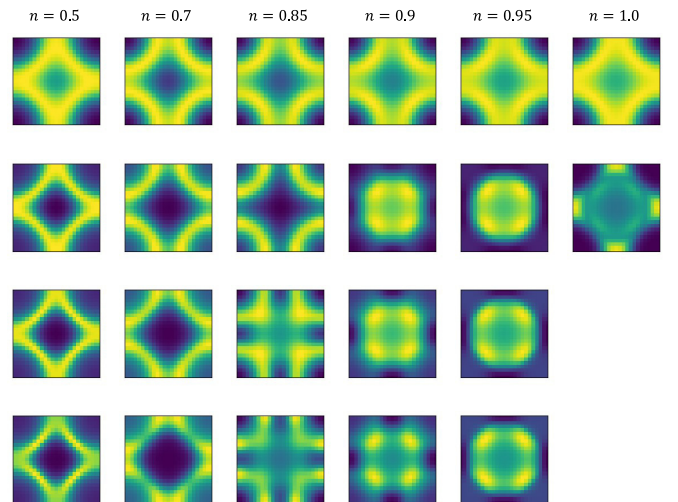


FIG. 3. The plot of $dn_k/d\mu$ for $U = 6.0$ and $t' = -0.25$ for 24×24 lattice. From left to right, the charge fillings are 0.5, 0.7, 0.85, 0.9, 0.95, 1.0. From top to bottom, the inverse temperatures are 1.0, 3.0, 5.0, and 8.0.

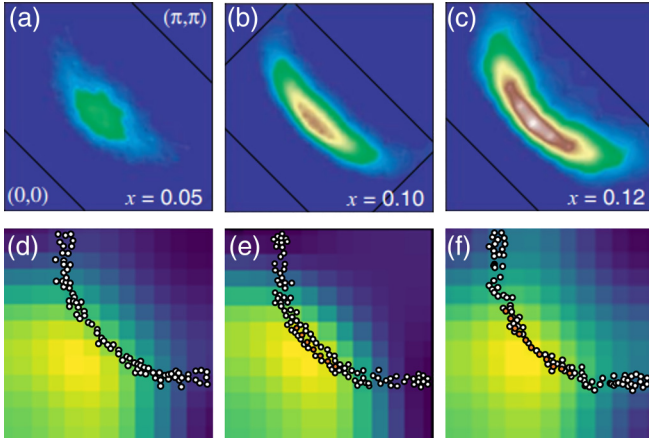


FIG. 4. Comparison of Fermi arc with the experimental results of $\text{Ca}_{2-x}\text{Na}_x\text{CuO}_2\text{Cl}_2$ in Ref. [21]. The experimental results are replotted in (a)–(f). (a)–(c) show the distribution of spectral weight in the Brillouin zone within a ± 10 meV window around the Fermi energy for $x = 0.05, 0.10$, and 0.12 in one quadrant of the first Brillouin zone. The backgrounds of (d)–(f) are our numerical results at the same dopings, and the circles are experimental results used to detect the FS contours. Note that the distribution of the circles in (d)–(f) has some deviation from the experimental results, but the position of the Fermi arc is ensured.

Ref. [21]. We use the same model parameters as before ($U = 6.0$ and $t' = -0.25$) and a 24×24 lattice size. Figure 4 shows that our results are not quantitatively satisfactory for small doping levels ($x = 0.05$), but for doping levels of 0.1 and 0.12 , the shape and position of the Fermi arc are in good quantitative agreement with the experimental results.

In Fig. 3, it is evident that the Fermi surface undergoes topological transitions as a function of charge filling, passing through several stages. To highlight these transitions more clearly, we present a series of surfaces for slowly varying fillings with a fixed temperature of $1/T = 3.0$, as shown in Fig. 5. At low fillings, the Fermi surface is electronlike, cen-

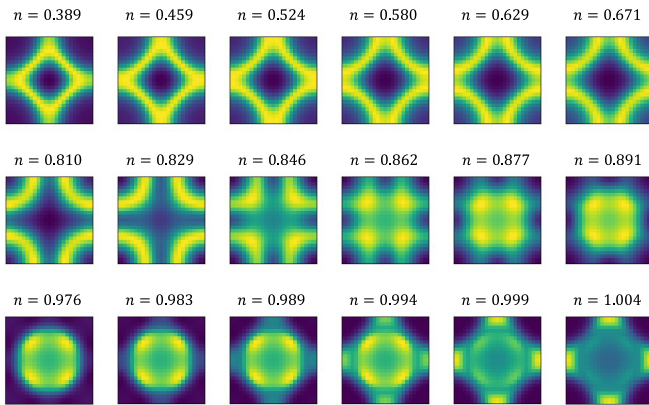


FIG. 5. The topological transition of the Fermi surface with increasing filling number for fixed temperature $1/T = 3.0$. The top panel shows the transition from an electronlike surface to a holelike surface. The middle panel shows the transition from a closed surface to a Fermi arc. The bottom panel shows the transition from a Fermi arc to a Mott insulatorlike feature.

tered at $(0, 0)$, and the system is typically regarded as a Fermi liquid. As the filling increases, the electronlike Fermi surface begins to touch the boundary of the first Brillouin zone, becoming holelike. This transition can still be considered as a Fermi liquid and is likely due to the next-nearest-neighbor hopping strength t' . Upon further increasing the filling, the position of the Fermi surface slows down, and at the junction of the Fermi surface and the first Brillouin zone, the zero-frequency intensity begins to decrease, indicating the onset of the pseudogap. This leads to blurring of the Fermi surface in that area and the appearance of the Fermi arc. The Fermi arc shortens with increasing filling until it almost shrinks to a point near the node $(\frac{\pi}{2}, \frac{\pi}{2})$. Finally, the system enters the Mott phase, where the gap is fully opened.

B. View on pseudogap

The *HGW* method is essentially a weak coupling fluctuation theory, so its view on the pseudogap is similar to that of TPSC theory [18]. Specifically, when the spin fluctuations are strong, the effective two-body potential $W_{\sigma\bar{\sigma}}(iq^0 = 0, \mathbf{q})$ is proportional to the RPA-like spin density correlation function:

$$W_{\sigma\bar{\sigma}}(0, \mathbf{q}) = -\frac{U^2 \chi_0(\mathbf{q})}{1 - U^2 \chi_0^2(\mathbf{q})} \sim -\frac{1}{2} U^2 \chi^{rmsp}(\mathbf{q}), \quad (15)$$

with the asymmetric bare correlator

$$\chi_0(\mathbf{q}) = -\frac{1}{\beta L^2} \sum_{ik^0, \mathbf{k}} H(ik^0, \mathbf{k} + \mathbf{q}) G(ik^0, \mathbf{k}) \quad (16)$$

and the RPA-like spin density correlation function

$$\chi^{sp}(\mathbf{q}) = \frac{\chi_0(\mathbf{q})}{1 - U \chi_0(\mathbf{q})}. \quad (17)$$

Our numerical calculation (see Appendix B) for the minus of $W_{\sigma\bar{\sigma}}(0, \mathbf{q})$ shows that it peaks at a momentum \mathbf{Q} near (π, π) when the system is at near half-filling.

Consider the case $\mathbf{Q} = (\pi, \pi)$ and assume

$$\frac{1}{\beta L^2} W_{\sigma\bar{\sigma}}(iq^0, \mathbf{q}) \sim -\gamma^2 \delta_{q^0, 0} \delta_{\mathbf{q}, \mathbf{Q}}. \quad (18)$$

The inverse Green's function then takes the form

$$G^{-1}(ik^0, \mathbf{k}) = -ik^0 + (\varepsilon_{\mathbf{k}} - \mu') + \frac{\gamma^2}{-ik^0 + (\varepsilon_{\mathbf{k}+\mathbf{Q}} - \mu')}, \quad (19)$$

with μ' the renormalized chemical potential. This expression shows the similarity with the antiferromagnetic (AFM) mean-field theory [28]. For this reason, the *HGW* method can qualitatively capture the AFM gap. Equation (19) also allows the onset of the hole pocket, which is not detected by our numerical calculation. The emergence of the pseudogap and the difficulty in detecting the hole pocket can be attributed to the nonlocal correlation effect and the dynamical effect of the spin correlation function, which depends on both momentum and Matsubara frequency.

V. SUMMARY

The importance of FS is not only due to its connection with strongly correlated effects, but also an important quantity to

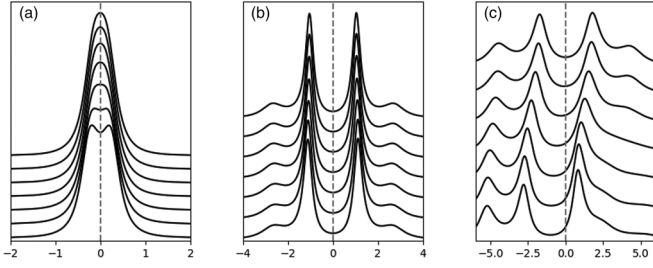


FIG. 6. The spectral function along the antinode to the node at half-filling for (a) $U = 2$, $t' = 0$, $\beta = 6.6$, (b) $U = 4$, $t' = 0$, $\beta = 5.0$, and (c) $U = 6$, $t' = -0.25$, $\beta = 3.0$.

verify the matching of models and methods with the experiments. However, at present, few many-body methods can well simulate FS, due to the NAC's difficulty or other factors. To this end, we provide a new notion, the momentum-dependent compressibility $dn_k/d\mu$, to determine the effective FS. We have done theoretical analytical and numerical verification on the similarity between the effective FS and the common FS determined by the maximum intensity method. Considering that for many numerical approaches, it is much more difficult to calculate the dynamical Green's function $G(ik^0, \mathbf{k})$ or $G(\tau, \mathbf{k})$ than the static momentum distribution n_k , the effective FS will be very beneficial.

In addition, the *HGW* method, used as the testing solver, shows the change process of FS with the increase of fillings from Fermi liquid state to Mott state. These results can qualitatively match with the experiments. Besides, from the perspective of the *HGW* method, the strong spin fluctuation is the origin of the pseudogap, which is consistent with the mainstream [29].

It is also worth noting that, in addition to FS contour, the spectral intensity $A(\omega = 0, \mathbf{k})$ is also significant. Our work has shown its connection to the momentum-dependent compressibility, and thus the charge density correlation function. The spectral intensity might also be related to the charge transport properties.

APPENDIX A: METHODOLOGY

The *HGW* method we use for numerical computation is based on the truncation of correlation functions of the Dyson-Schwinger equations. To formulate this method, we first write down the Matsubara action in the path integral formalism:

$$\begin{aligned} \mathcal{A}[\psi, \psi^*] = & - \sum_{\sigma} \int_{12} \psi_{\sigma}^*(1) T_{\sigma}(1, 2) \psi_{\sigma}(2) \\ & + \frac{U}{2} \sum_{\sigma} \int_1 n_{\sigma}(1) n_{\bar{\sigma}}(1) + \int_1 \phi_{\sigma}(1) n_{\sigma}(1). \end{aligned} \quad (\text{A1})$$

Here the label $1 \equiv (\mathbf{x}_1, \tau_1)$ indicates the lattice coordinate \mathbf{x}_1 and the Matsubara time τ_1 . $\psi_{\sigma}(1)$ is the electronic field with z spin σ at lattice coordinate \mathbf{x}_1 and Matsubara time τ_1 . $n_{\sigma}(1) \equiv \psi_{\sigma}^*(1) \psi_{\sigma}(1)$ is the spin-selective charge density operator, noting that $n_{\uparrow}(1) - n_{\downarrow}(1)$ is the z -spin density operator and $n_{\uparrow}(1) + n_{\downarrow}(1)$ is the total charge density operator. $T_{\sigma}(1, 2)$ is the inverse noninteracting Green's function, and U is the on-site Coulomb repulsive interaction strength. An

TABLE I. Antinodal and nodal gaps for different U 's.

U	2.0	3.0	4.0	5.0	6.0
$1/T$	8.0	7.0	5.0	3.0	3.0
gap AN	0.594	1.35	1.96	2.73	3.14
gap N	0.536	1.28	1.82	2.46	2.82

external bosonic source $\phi_{\sigma}(1)$ coupled to $n_{\sigma}(1)$ is introduced in our formalism, and will be set to zero in the numerical calculations. Note that $\phi_{\uparrow}(1) - \phi_{\downarrow}(1)$ corresponds to the magnetic field in the z direction and $\phi_{\uparrow}(1) + \phi_{\downarrow}(1)$ corresponds to the minus chemical potential.

The Matsubara Green's function is defined as:

$$G_{\sigma}(1, 2) = -\langle \psi_{\sigma}(1) \psi_{\sigma}^*(2) \rangle. \quad (\text{A2})$$

Here $\langle \dots \rangle$ is the ensemble average. The equation of motion takes the form:

$$0 = \int_3 H_{\sigma}^{-1}(1, 3) G_{\sigma}(3, 2) + U \frac{\delta G_{\sigma}(1, 2)}{\delta \phi_{\bar{\sigma}}(1)}. \quad (\text{A3})$$

Note that the quantity $\delta G_{\sigma}(1, 2)/\delta \phi_{\sigma'}(3)$ means the variation of the Matsubara Green's function $G_{\sigma}(1, 2)$ with the external source $\phi_{\sigma'}(3)$, and satisfies:

$$\begin{aligned} \frac{\delta G_{\sigma}(1, 2)}{\delta \phi_{\sigma'}(3)} = & -\langle \psi_{\sigma}(1) \psi_{\sigma'}^*(2) \psi_{\sigma'}(3) \psi_{\sigma}^*(3) \rangle \\ & + G_{\sigma}(1, 2) G_{\sigma'}(3, 3). \end{aligned} \quad (\text{A4})$$

The quantity $H_{\sigma}(1, 2)$ is called the Hartree propagator, which is the noninteracting Green's function containing the Hartree self-energy

$$H_{\sigma}^{-1}(1, 2) = T_{\sigma}(1, 2) - \delta(1, 2) \phi_{\sigma}(1) - U \delta(1, 2) G_{\bar{\sigma}}(1, 1). \quad (\text{A5})$$

By functional derivative of Eq. (A3) with respect to ϕ , one obtains

$$\frac{\delta}{\delta \phi_{\sigma'}(3)} \left[\int_4 H_{\sigma}^{-1}(1, 4) G_{\sigma}(4, 2) \right] = -U \frac{\delta^2 G_{\sigma}(1, 2)}{\delta \phi_{\sigma'}(3) \delta \phi_{\bar{\sigma}}(1)}. \quad (\text{A6})$$

Truncation would be made on Eq. (A6) to form a closed system of equations.

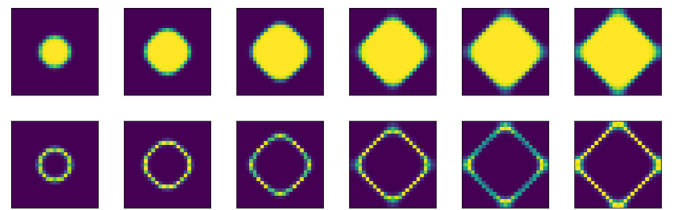


FIG. 7. The plot of momentum distribution function n_k (top), and momentum-dependent compressibility $dn_k/d\mu$ (bottom) for $U = 0$ and $t' = 0$. From left to right, the fillings are 0.2, 0.4, 0.6, 0.8, 0.9, 1.0.

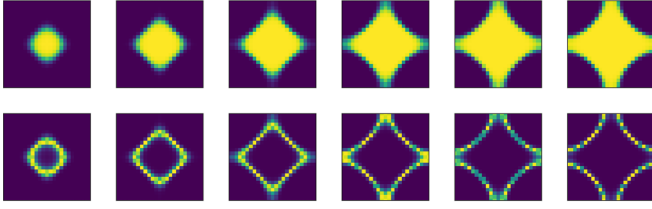


FIG. 8. The plot of momentum distribution function n_k (top), and momentum-dependent compressibility $dn_k/d\mu$ (bottom) for $U = 0$ and $t' = -0.25$. From left to right, the fillings are 0.2, 0.4, 0.6, 0.8, 0.9, 1.0.

1. *HGW* equations for Green's function

Equation (A3) shows a relationship between the Green's function G and its derivative $\delta G/\delta\phi$, and Eq. (A6) relates $\delta G/\delta\phi$ to a higher-order derivative $\delta^2 G/\delta\phi^2$. We truncate $\delta^2 G/\delta\phi^2$ in Eq. (A6) due to the clustering property of correlation functions. Then Eq. (A6) becomes

$$\frac{\delta G_\sigma(1, 2)}{\delta\phi_{\sigma'}} = - \int d(45) H_\sigma(1, 4) \frac{\delta H_\sigma^{-1}(4, 5)}{\delta\phi_{\sigma'}} G(5, 2). \quad (\text{A7})$$

Arranging Eqs. (A3), (A5), (A7), then one obtains the *HGW* equations:

$$G_\sigma^{-1}(1, 2) = H_\sigma^{-1}(1, 2) + H_\sigma(1, 2) W_{\sigma\bar{\sigma}}(2, 1), \quad (\text{A8a})$$

$$[W^{-1}]_{\sigma\sigma'}(1, 2) = \frac{1}{U} \delta_{\sigma\sigma'} - \delta_{\bar{\sigma}\sigma'} H_{\bar{\sigma}}(1, 2) G_\sigma(2, 1). \quad (\text{A8b})$$

For translational invariant systems in absence of external source, the *HGW* equations read

$$G_\sigma^{-1}(k) = H_\sigma^{-1}(k) + \frac{1}{\mathcal{N}} \sum_q H_\sigma(k+q) W_{\sigma\bar{\sigma}}(q) \quad (\text{A9a})$$

$$[W^{-1}]_{\sigma\sigma'}(q) = \frac{1}{U} \delta_{\sigma\sigma'} - \frac{1}{\mathcal{N}} \sum_k H_\sigma(k+q) G_{\bar{\sigma}}(k) \quad (\text{A9b})$$

with $H_\sigma^{-1}(k) = T_\sigma(k) - \frac{U}{\mathcal{N}} \sum_p G_{\bar{\sigma}}(p)$. Here \mathcal{N} is a normalization factor.

2. Calculation of momentum-dependent compressibility

The momentum-dependent compressibility is defined as the derivative of momentum distribution function $n_k \equiv \frac{1}{\beta} \sum_{n,\sigma} G_\sigma(\mathbf{k}, i\omega_n)$ with respect to the chemical potential. One can calculate the Green's function $G_\sigma(\mathbf{k}, i\omega_n; \mu)$ for different chemical potentials μ . By definition, the momentum-dependent compressibility equals to

$$\frac{dn_k}{d\mu} = \lim_{\Delta\mu \rightarrow 0} \frac{1}{\beta} \sum_{n,\sigma} \frac{G_\sigma(\mathbf{k}, i\omega_n; \mu + \Delta\mu) - G_\sigma(\mathbf{k}, i\omega_n; \mu)}{\Delta\mu}. \quad (\text{A10})$$

Then one obtains $dn_k/d\mu$ by the numerical differentiation.

Besides, one can also calculate $dn_k/d\mu$ using the functional derivative scheme. Take μ as a variable, and note that

$\delta T_\sigma(k) = \delta\mu$. The variation of Eq. (A9a) is

$$\begin{aligned} \delta G_\sigma^{-1}(k) &= \delta H_\sigma^{-1}(k) + \frac{1}{\mathcal{N}} \sum_q \delta H_\sigma(k+q) W_{\sigma\bar{\sigma}}(q) \\ &+ \frac{1}{\mathcal{N}} \sum_q H_\sigma(k+q) \delta W_{\sigma\bar{\sigma}}(q), \end{aligned} \quad (\text{A11})$$

the variation of $H_\sigma^{-1}(k)$ is

$$\delta H_\sigma^{-1}(k) = \delta\mu - \frac{U}{\mathcal{N}} \sum_p \delta G_{\bar{\sigma}}(p), \quad (\text{A12})$$

and the variation of Eq. (A9b) is

$$\begin{aligned} \delta[W^{-1}]_{\sigma\sigma'}(q) &= -\frac{\delta_{\bar{\sigma}\sigma'}}{\mathcal{N}} \sum_q \delta H_{\bar{\sigma}}(k+q) G_\sigma(k) \\ &- \frac{\delta_{\bar{\sigma}\sigma'}}{\mathcal{N}} \sum_q H_{\bar{\sigma}}(k+q) \delta G_\sigma(k). \end{aligned} \quad (\text{A13})$$

Letting $\Lambda_\sigma(k) \equiv -\delta G_\sigma^{-1}(k)/\delta\mu$ and $\Lambda_\sigma^H(k) \equiv -\delta H_\sigma^{-1}/\delta\mu$, one obtains

$$\Lambda_\sigma(k) = \Lambda_\sigma^H(k) + \Lambda_\sigma^{\text{MT}}(k) + \Lambda_\sigma^{\text{AL}}(k), \quad (\text{A14})$$

with the Maki-Thompson component

$$\Lambda_\sigma^{\text{MT}}(k) = \frac{1}{\mathcal{N}} \sum_q H_\sigma(k+q) H_\sigma(k+q) W_{\sigma\bar{\sigma}}(q) \Lambda_\sigma^H(k+q), \quad (\text{A15})$$

and the Aslamazov-Larkin component

$$\Lambda_\sigma^{\text{AL}}(k) = \frac{1}{\mathcal{N}} \sum_{q, \sigma_1, \sigma_2} H_\sigma(k+q) W_{\sigma\sigma_1}(q) W_{\sigma_2\bar{\sigma}}(q) \Gamma_{\sigma_1\sigma_2}(q), \quad (\text{A16})$$

with $\Gamma_{\sigma_1\sigma_2}(q) \equiv -\delta[W^{-1}]_{\sigma_1\sigma_2}(q)/\delta\mu$. From Eq. (A13), one obtains

$$\begin{aligned} \Gamma_{\sigma\sigma'}(q) &= -\frac{\delta_{\bar{\sigma}\sigma'}}{\mathcal{N}} \sum_q H_{\bar{\sigma}}(k+q) H_{\bar{\sigma}}(k+q) G_\sigma(k) \Lambda_{\bar{\sigma}}^H(k+q) \\ &- \frac{\delta_{\bar{\sigma}\sigma'}}{\mathcal{N}} \sum_q H_{\bar{\sigma}}(k+q) G_\sigma(k) G_{\sigma'}(k) \Lambda_\sigma(k). \end{aligned} \quad (\text{A17})$$

Then $\Lambda_\sigma(k)$ can be obtained by solving the vertex equations Eq. (A14), and thus the variation of the Green's function $G_\sigma(k)$ with respect to the chemical potential μ

$$\frac{\delta G_\sigma(k)}{\delta\mu} = G_\sigma(k) G_\sigma(k) \Lambda_\sigma(k), \quad (\text{A18})$$

can be calculated. The momentum-dependent compressibility $dn_k/d\mu$ is then carried out.

3. Discretized Matsubara time path integral formalism

For numerical implementation, we use the discretized Matsubara time path integral formalism where the Matsubara time length β is divided into finite M pieces of intervals. The action

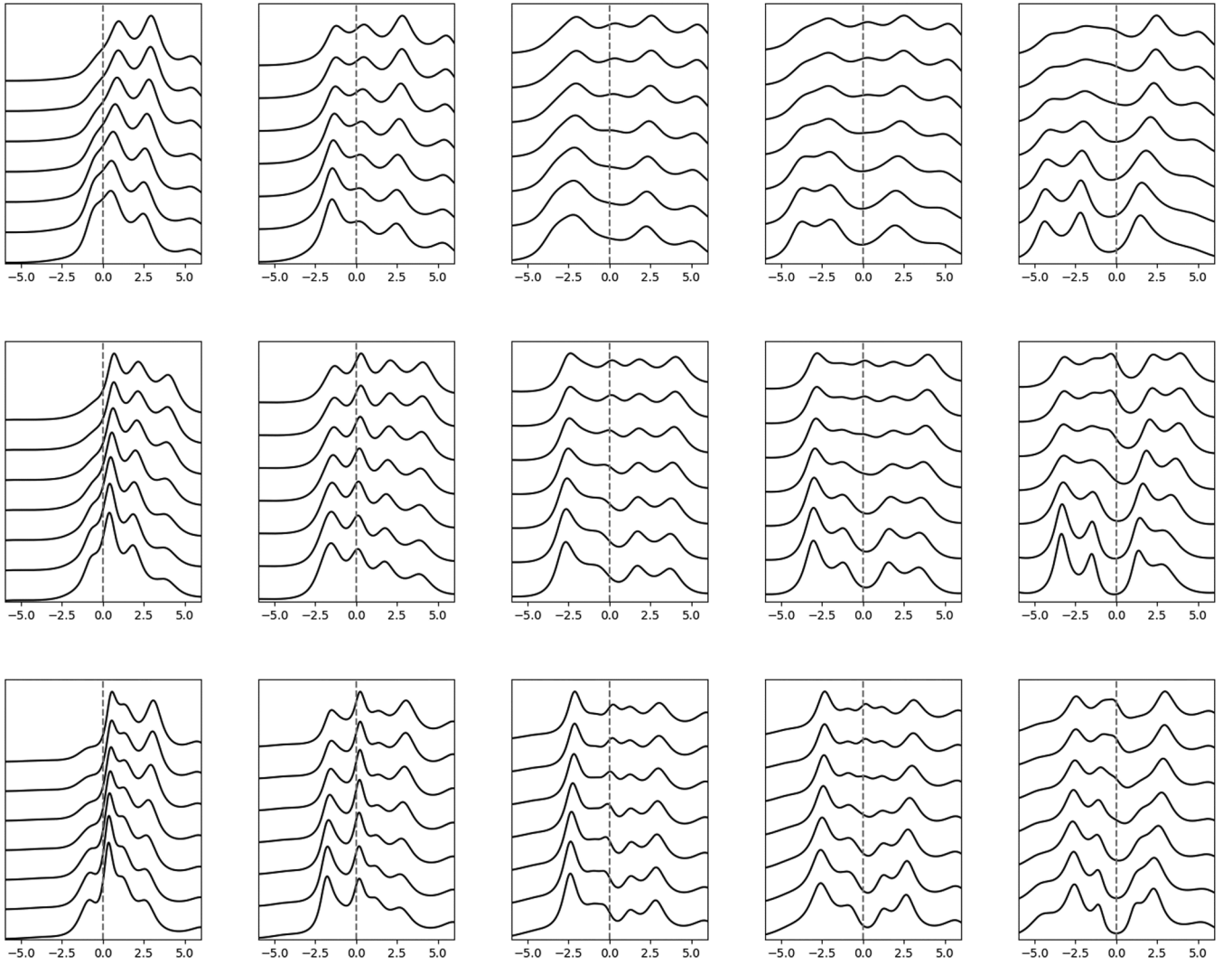


FIG. 9. The plot of FS determined by the maximum intensity method for $U = 6.0$ and $t = -0.25$ for 24×24 lattice. From left to right, the charge fillings are 0.5, 0.7, 0.85, 0.9, 0.95. From top to bottom, the inverse temperatures are 3.0, 5.0, and 8.0.

with finite M for the $L \times L$ Hubbard model takes the form

$$\mathcal{A}_M[\psi, \psi^*] = - \sum_{\sigma, x, x', l, l'} \psi_{\sigma}^*(x\tau_l) T_{\sigma}(x\tau_l, x'\tau_{l'}) \psi_{\sigma}(x'\tau_{l'}) + \frac{U}{2} \Delta\tau \sum_{\sigma} \sum_{xl} n_{\sigma}(x, \tau_l) n_{\bar{\sigma}}(x\tau_l). \quad (\text{A19})$$

Here x indicates the lattice site, $\tau_l \equiv l\Delta\tau$ refers to the Matsubara time and $\Delta\tau = \beta/M$ is the length of integral. As M tends to infinity, the summation $\Delta\tau \sum_{l=0}^{M-1}$ becomes the integral $\int_0^{\beta} d\tau$, i.e., the continuous Matsubara time limit.

The Hamiltonian for the Hubbard model reads

$$\mathcal{H} = - \sum_{\sigma, x, x'} t_{xx'} c_{\sigma, x}^{\dagger} c_{\sigma, x'} + \frac{U}{2} \sum_{\sigma, x} n_{\sigma, x} n_{\bar{\sigma}, x} - \mu \sum_{\sigma, x} n_{\sigma, x}. \quad (\text{A20})$$

Here $c_{\sigma x}^{\dagger}$ ($c_{\sigma x}$) is the creation (annihilation) operator for the fermion at lattice site x with z spin σ , and $n_{\sigma x} \equiv c_{\sigma x}^{\dagger} c_{\sigma x}$ is the density operator. $t_{xx'}$ is the hopping strength between sites x and x' . The corresponding inverse noninteracting Green's

function is then:

$$T_{\sigma}(x\tau_l, x'\tau_{l'}) = \Delta\tau \left(-\frac{1}{\Delta\tau} \delta_{xx'} (\delta_{l, l'-1} - \delta_{l, l'}) + t_{xx'} \delta_{l, l'} + \mu \delta_{xx'} \delta_{l, l'} \right). \quad (\text{A21})$$

Due to the antiperiodicity at the Matsubara time axis, the Fermionic arraylike quantity X_F takes the form:

$$X_F(x\tau_l, x'\tau_{l'}) = \frac{1}{\mathcal{N}} \sum_{k, m} X_F(k, m) e^{ik \cdot (x-x')} e^{i \frac{2m+1}{M\beta} \pi (\tau_l - \tau_{l'})}. \quad (\text{A22})$$

Due to the periodicity, the Bosonic arraylike quantity X_B takes the form:

$$X_B(x\tau_l, x'\tau_{l'}) = \frac{1}{\mathcal{N}} \sum_{k, m} X_B(k, m) e^{ik \cdot (x-x')} e^{i \frac{2m}{M\beta} \pi (\tau_l - \tau_{l'})}. \quad (\text{A23})$$

The normalization factor \mathcal{N} equals to the number of values of (k, m) , i.e., $\mathcal{N} = ML^2$. Note that $T_{\sigma}(x\tau_l, x'\tau_{l'})$ is a Fermionic

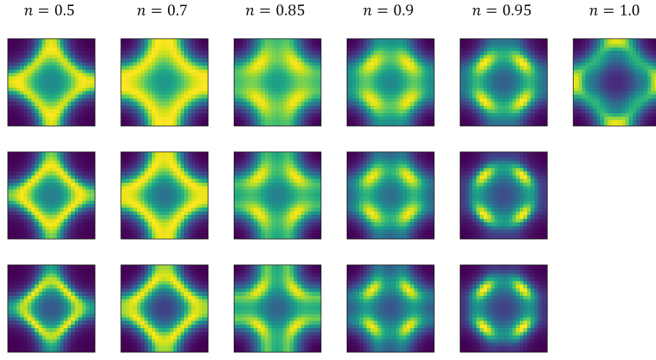


FIG. 10. The plot of FS determined by the maximum intensity method for $U = 6.0$ and $t = -0.25$ for 24×24 lattice. From left to right, the charge fillings are 0.5, 0.7, 0.85, 0.9, 0.95, 1.0. From top to bottom, the inverse temperatures are 3.0, 5.0, and 8.0.

quantity, and its Fourier transformation equals to:

$$T_{\sigma}(\mathbf{k}, m) = \Delta\tau \left(-\frac{1}{\Delta\tau} (e^{-i\frac{2m+1}{M}\pi} - 1) - (\varepsilon_{\mathbf{k}} - \mu) \right). \quad (\text{A24})$$

Here $\varepsilon_{\mathbf{k}}$ is the noninteracting dispersion. Noting that if $m/M \ll 1$, $-\frac{1}{\Delta\tau}(e^{-i\frac{2m+1}{M}\pi} - 1) \rightarrow i\pi(2m+1)/\beta$, i.e., the Matsubara frequency in the continuous time limit.

APPENDIX B: SUPPORTING NUMERICAL RESULTS

1. Quality of the *HGW* method: Spectral functions and gaps

Here we display the spectral function in Fig. 6 along the antinode $(\pi, 0)$ to the node $(\pi/2, \pi/2)$ at half-filling for

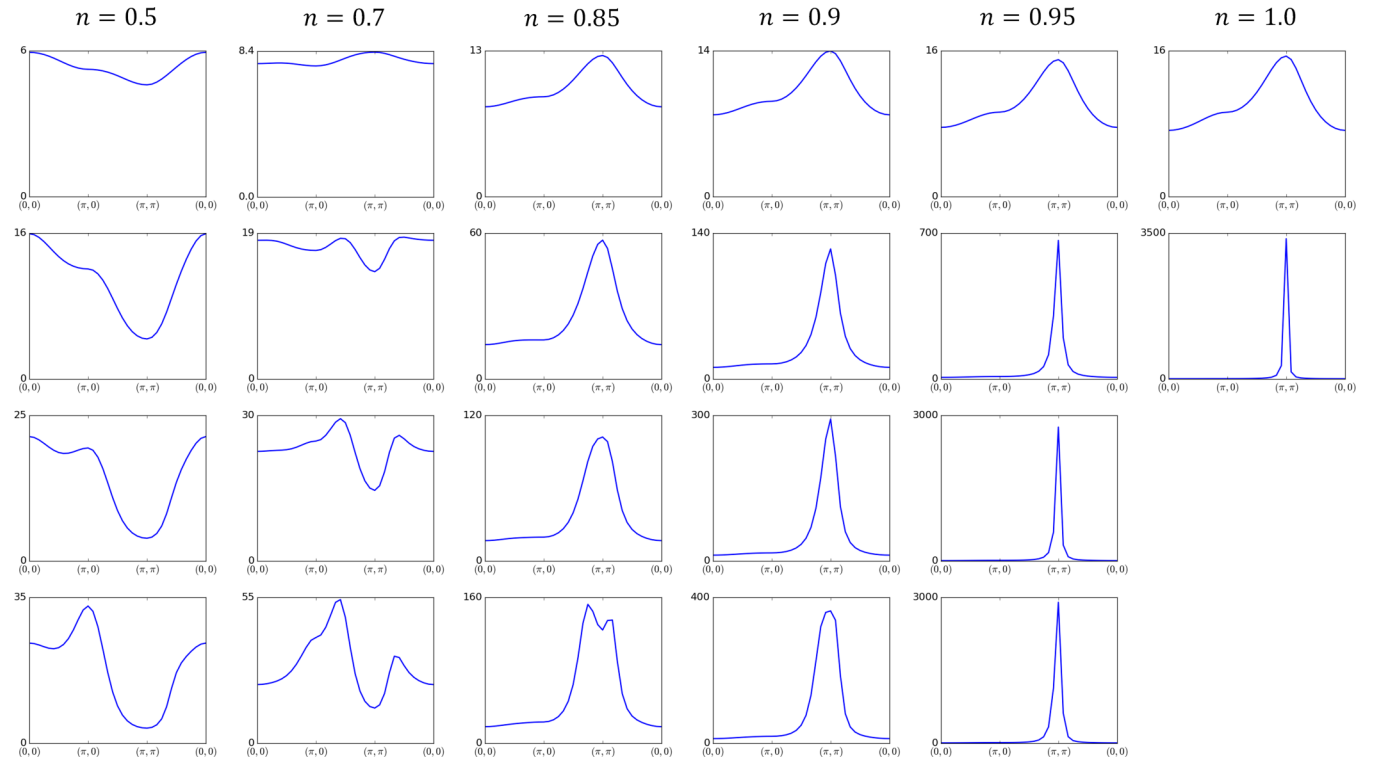


FIG. 11. The plot of the minus of $W_{\sigma\sigma}(iq^0 = 0, \mathbf{q})$ for $U = 6.0$ and $t = -0.25$ for 24×24 lattice. From left to right, the charge fillings are 0.5, 0.7, 0.85, 0.9, 0.95, 1.0. From top to bottom, the inverse temperatures are 1.0, 3.0, 5.0, and 8.0.

[Fig. 6(a)] $U = 2$, $t' = 0$, $\beta = 6.6$, [Fig. 6(b)] $U = 4$, $t' = 0$, $\beta = 5.0$, and [Fig. 6(c)] $U = 6$, $t' = -0.25$, $\beta = 3.0$. Figure 6(a) shows the onset of double peaks, indicating the end of the pseudogap. The critical temperature is about $T = 0.151$, much higher than 0.065 given by the Monte Carlo [29]. Figure 6(b) shows a deep valley between two peaks, indicating the nearly Mott phase. The gap between two peaks is about 2.0, larger than 1.4 given by the Monte Carlo for 8×8 cluster. Figure 6(c) indicates the nearly Mott phase, and also displays some high-energy excitations.

We further list the antinodal gap and the nodal gap for different U 's and $t' = 0$ in the Table I. The second line $1/T$ means the inverse temperature used. Compared with the results obtained by DQMC, our results obviously overestimate the energy gaps. These results give us the positioning of the *HGW* method: it qualitatively captures the pseudogap and the Mott gap, whereas is not quantitatively very good. Therefore, we expect that the *HGW* method can qualitatively describe the physics related to the pseudogap.

2. Noninteracting FS topology

We display the surface topology changes with the charge fillings for $U = 0$ model on a 24×24 lattice in Fig. 7 for $t' = 0$ and Fig. 8 for $t' = -0.25$. For $U = 0$ and $t' = 0$, the surface topology is similar to the weak coupling $U = 2$ and intermediate coupling $U = 4$ shown in the main text. For $U = 0$ and $t' = -0.25$, the surface exhibits a transition from the electronlike one to the holelike one, but does not exhibit the arc and Mott feature.

3. Spectral functions and FS for $U = 6.0$ and $t' = -0.25$

We plot the spectral functions using the Nevanlinna analytical continuation procedure for different fillings and temperatures at $U = 6.0$ and $t' = -0.25$, as shown in Fig. 9. We further plot FS by the maximum spectral intensity method in Fig. 10. The results are similar to the surface determined by $dn_k/d\mu$ on the whole, also exhibit the arc features.

4. Effective potential in the HGW method

In the HGW method, the effective potential $W_{\sigma\bar{\sigma}}(iq^0 = 0, \mathbf{q})$ plays an important role in capturing the pseudogap physics. We plot the minus of $W_{\sigma\bar{\sigma}}(iq^0 = 0, \mathbf{q})$ for different parameters as shown in Fig. 11. At near half-filling, the quantity dominates at a momentum near (π, π) . The qualitative relationship between $W_{\sigma\bar{\sigma}}(iq^0, \mathbf{q})$ and the pseudogap has been described in the main text, but quantitative analysis would be very difficult.

-
- [1] M. R. Norman, H. Ding, M. Randeria, J. C. Campuzano, T. Yokoya, T. Takeuchi, T. Takahashi, T. Mochiku, K. Kadowaki, P. Guptasarma *et al.*, *Nature (London)* **392**, 157 (1998).
 - [2] I. Dzyaloshinskii, *Phys. Rev. B* **68**, 085113 (2003).
 - [3] C. Gros, B. Edegger, V. Muthukumar, and P. Anderson, *Proc. Natl. Acad. Sci. USA* **103**, 14298 (2006).
 - [4] J. Mesot, M. Randeria, M. R. Norman, A. Kaminski, H. M. Fretwell, J. C. Campuzano, H. Ding, T. Takeuchi, T. Sato, T. Yokoya, T. Takahashi, I. Chong, T. Terashima, M. Takano, T. Mochiku, and K. Kadowaki, *Phys. Rev. B* **63**, 224516 (2001).
 - [5] A. Damascelli, Z. Hussain, and Z.-X. Shen, *Rev. Mod. Phys.* **75**, 473 (2003).
 - [6] J. A. Sobota, Y. He, and Z.-X. Shen, *Rev. Mod. Phys.* **93**, 025006 (2021).
 - [7] M. Platé, J. D. F. Mottershead, I. S. Elfimov, D. C. Peets, R. Liang, D. A. Bonn, W. N. Hardy, S. Chiuzbaian, M. Falub, M. Shi, L. Patthey, and A. Damascelli, *Phys. Rev. Lett.* **95**, 077001 (2005).
 - [8] K. Tanaka, W. Lee, D. Lu, A. Fujimori, T. Fujii, Risdiana, I. Terasaki, D. Scalapino, T. Devereaux, Z. Hussain *et al.*, *Science* **314**, 1910 (2006).
 - [9] S. Benhabib, A. Sacuto, M. Civelli, I. Paul, M. Cazayous, Y. Gallais, M.-A. Méasson, R. D. Zhong, J. Schneeloch, G. D. Gu, D. Colson, and A. Forget, *Phys. Rev. Lett.* **114**, 147001 (2015).
 - [10] N. Doiron-Leyraud, O. Cyr-Choinière, S. Badoux, A. Ataei, C. Collignon, A. Gourgout, S. Dufour-Beauséjour, F. Tafti, F. Laliberté, M.-E. Boulanger *et al.*, *Nature Commun.* **8**, 2044 (2017).
 - [11] I. Vishik, *Rep. Prog. Phys.* **81**, 062501 (2018).
 - [12] K. Mitsen and O. Ivanenko, *J. Alloys Compd.* **791**, 30 (2019).
 - [13] T. A. Maier, T. Pruschke, and M. Jarrell, *Phys. Rev. B* **66**, 075102 (2002).
 - [14] W. Wu, M. S. Scheurer, S. Chatterjee, S. Sachdev, A. Georges, and M. Ferrero, *Phys. Rev. X* **8**, 021048 (2018).
 - [15] O. Gunnarsson, M. W. Haverkort, and G. Sangiovanni, *Phys. Rev. B* **81**, 155107 (2010).
 - [16] J. Fei, C.-N. Yeh, and E. Gull, *Phys. Rev. Lett.* **126**, 056402 (2021).
 - [17] Z. Sun, Z. Fan, H. Li, D. Li, and B. Rosenstein, *Phys. Rev. B* **104**, 125137 (2021).
 - [18] Y. M. Vilk and A. M. S. Tremblay, *Journal de Physique I* **7**, 1309 (1997).
 - [19] C. N. Varney, C.-R. Lee, Z. J. Bai, S. Chiesa, M. Jarrell, and R. T. Scalettar, *Phys. Rev. B* **80**, 075116 (2009).
 - [20] E. W. Huang, R. Sheppard, B. Moritz, and T. P. Devereaux, *Science* **366**, 987 (2019).
 - [21] K. M. Shen, F. Ronning, D. Lu, F. Baumberger, N. Ingle, W. Lee, W. Meevasana, Y. Kohsaka, M. Azuma, M. Takano *et al.*, *Science* **307**, 901 (2005).
 - [22] T. Yoshida, X. J. Zhou, K. Tanaka, W. L. Yang, Z. Hussain, Z.-X. Shen, A. Fujimori, S. Sahrakorpi, M. Lindroos, R. S. Markiewicz, A. Bansil, S. Komiya, Y. Ando, H. Eisaki, T. Kakeshita, and S. Uchida, *Phys. Rev. B* **74**, 224510 (2006).
 - [23] F. Ronning, C. Kim, D. Feng, D. Marshall, A. Loeser, L. Miller, J. Eckstein, I. Bozovic, and Z.-X. Shen, *Science* **282**, 2067 (1998).
 - [24] N. Doiron-Leyraud, C. Proust, D. LeBoeuf, J. Levallois, J.-B. Bonnemaison, R. Liang, D. Bonn, W. Hardy, and L. Taillefer, *Nature (London)* **447**, 565 (2007).
 - [25] S. Chakravarty, R. B. Laughlin, D. K. Morr, and C. Nayak, *Phys. Rev. B* **63**, 094503 (2001).
 - [26] X.-G. Wen and P. A. Lee, *Phys. Rev. Lett.* **76**, 503 (1996).
 - [27] K.-Y. Yang, T. M. Rice, and F.-C. Zhang, *Phys. Rev. B* **73**, 174501 (2006).
 - [28] J. E. Hirsch, *Phys. Rev. B* **31**, 4403 (1985).
 - [29] T. Schäfer, N. Wentzell, F. Šimkovic, Y.-Y. He, C. Hille, M. Klett, C. J. Eckhardt, B. Arzhang, V. Harkov, F.-M. Le Régent, A. Kirsch, Y. Wang, A. J. Kim, E. Kozik, E. A. Stepanov, A. Kauch, S. Andergassen, P. Hansmann, D. Rohe, Y. M. Vilk *et al.*, *Phys. Rev. X* **11**, 011058 (2021).